Electrical conductivity studies of anatase TiO2 with dominant highly reactive {0 0 1} facets

K. Pomoni[a,*], M.V. Sofianou[b], T. Georgakopoulos[a], N. Boukos[b], C. Trapalis[b]

[a]Department of Physics, University of Patras, 26504 Patras, Greece

[b]Institute of Advanced Materials, Physicochemical Processes, Nanotechnology and Microsystems, National Center for Scientific Research ‘‘Demokritos’’, 15310 Ag. Paraskevi Attikis, Greece

[*]K. Pomoni

Department of Physics, University of Patras, 26504 Patras, Greece

Tel.: +30 2610 997482

fax: +30 2610 997498.

E-mail address: pomoni@physics.upatras.gr

Abstract

Nanostructured powders of titanium dioxide anatase nanoplates with dominant highly reactive {0 0 1} facets were fabricated using a solvothermal method. Two kinds of samples, as prepared and calcinated at 600 °C, were studied using X-ray diffraction (XRD), transmission electron microscopy (TEM), and electrical conductivity in vacuum and in air. The dependence of the conductivity versus the inverse of temperature in the temperature range 150–440 K indicated the contribution of at least two conduction mechanisms in vacuum. The electron transport was controlled by partially depleted of charge carriers grains and adiabatic small polaron conduction in the high temperature regime and by Mott variable-range hopping (VRH) at lower temperatures. The environment was found from the experimental results to influence significantly the electrical conductivity values and its temperature dependence. A decrease with temperature in air is observed in the ranges 290–370 and 285–330 K for the as prepared and the calcinated sample respectively. Potential barriers caused by partial depletion of carriers at grain boundaries control the electrical conductivity behavior in air at high temperatures and VRH in the lower temperature regime.

Keywords

Anatase; TiO2; {0 0 1} facets; Electrical conductivity

1. Introduction

Titanium dioxide (TiO_2) is one of the most widely used metal oxides due to its unique properties. Its high chemical stability, non-toxicity, high refractive index, high photocatalytic activity, and low production cost make it one of the most interesting materials for applications ranging from optics to gas sensors via solar energy [1]. Significant efforts have been made for the modification of its electronic and optical

properties in order to extend the absorption to the visible light region, since the large band gap of TiO_2 (3.0–3.2 eV) limits its activity in ultraviolet (UV) region. They include the band gap modification by creating oxygen vacancies and oxygen sub-stoichiometry, by nonmetals including co-doping of nonmetals and metals doping [2-10].

The latest trends in the scientific research are focused on physical techniques of the photocatalyst modification and in particular on appropriate morphological modification of the semiconductor in order to enhance the photocatalyst effectiveness in the UV–visible range. The manufacture of nanostructured titania with regular porosity [11]; [12-14] or the formation of anatase titania nanocrystals with {0 0 1} facets that exhibit increased photoactivity [15-21] have attracted considerable attention in the last years. The intriguing surface and electronic properties of {0 0 1} – faceted anatase titania have a substantial effect on the surface separation and transfer of nanocrystals with photogenerated electron–hole pairs, resulting in a significant improvement of quantum efficiency of surface-mediated photocatalytic redox reactions [22]. Moreover, nanosheets, known as an important category of nanomaterials with a large surface area and an ultra thin thickness have many applications in nanodevices, photocatalysis, photoluminescence, and battery materials [23].

TiO_2 nanosheets, among other sheet-like semiconducting oxides nanomaterials, are attractive for their ultimate two-dimensionality with the thickness of subnano- to nanometer range, high crystallinity, well-defined composition, and novel or enhanced physical properties [24]. Layered TiO_2 with reactive {0 0 1} facets have shown excellent photocatalytic activity, resulting from the synergetic effects of the layered structure and the {0 0 1} facet-dominated nanosheets [21].

A significant effort has been achieved in the synthesis and assembly of anatase titania nanocrystals with {0 0 1} facets and an important number of different groups have focused on its high photocatalytic activity. Moreover, a fundamental understanding of the electrical properties in TiO_2 nanosheets is also important. Several of the technological applications of TiO_2, like the efficiency and performance of various optoelectronic devices depend on its considerable electrical and optical properties [25]. The temperature dependence of the conductivity is essential for obtaining significant information on charge transport mechanisms in TiO_2, which mechanisms depend on the structure and the measurement temperature region.

Based on the literature review, there has been no report on the electrical conductivity behavior of anatase TiO_2 nanoplates with reactive {0 0 1} facets. The aim of the present work is to study the structural and electrical properties of anatase TiO_2 nanoplates with reactive {0 0 1} facets and discuss the influence of the environment.

2. Experimental details

2.1. Preparation of TiO_2 nanoplates

Two kinds of samples were prepared. The first were as prepared TiO_2 anatase nanoplates with exposed {0 0 1} crystal facets and the second resulted after a calcination treatment of these nanoplates at 600 °C. All samples were prepared using a solvothermal method. In a typical synthesis for TiO_2 anatase nanoplates, 3 mmol of titanium isopropoxide [$Ti(C_3H_7O)_4$] from Alfa Aesar Chemicals was dissolved into 50 ml of absolute ethanol from Merck under vigorous stirring at room temperature. An amount of 0.6 ml (0.03 mol) hydrofluoric acid (HF 40%) from Merck was added into the ethanol solution as a capping agent. Then the solution was poured into a 60 ml

Teflon-lined autoclave until 80% of the volume was filled and was placed into the oven for 24 h at 180 °C.

All as-synthesized powder products were collected through centrifugation of the solutions and washed 3 times with distilled water and dried in a furnace at 70 °C overnight. Some of the dried samples were calcinated in static air in a Muffle furnace for 90 min at 600 °C with a ramping rate of 5 °C/min, according to the literature, in order to remove the adsorbed fluoride atoms from the {0 0 1} crystal facets of the TiO_2 anatase nanoplate. The samples were then cooled to room temperature.

2.2. X-ray diffraction (XRD) and transmission electron microscopy (TEM)

The crystalline phase of the TiO_2 anatase nanoplates were investigated by X-ray diffractometry (SIEMENS D500 diffractometer) using CuKα radiation. The measurements were performed using the following combination of slits: 1.0°/1.0°/1.0° as aperture diaphragms, 0.15° as detector diaphragm, and 0.15° as diffracted beam monochromator diaphragm. The measured 2θ range between 20° and 90° was scanned in steps of 0.03°/5 s. The accelerating voltage and applied current were 40 kV and 35 mA, correspondingly. The identification of the patterns was made by the cards of the International Centre for Diffraction Data.

The shape and the crystal structure were observed with a transmission electron microscope (Philips CM20) operated at 200 kV and equipped with a Gatan GIF200 image filter. The TEM specimens of the TiO2 anatase structures were prepared by direct deposition on a carbon coated Cu TEM grid.

2.3. Electrical conductivity measurements

The electrical characterization was performed using DC conductivity measurements. The conductivity of the samples was measured as a function of temperature in different ambient environment, in vacuum and in air. The measurements were carried out in a vacuum cryostat using a bias voltage of 5 V and the resulting current was measured by a Keithley 6517A electrometer, while the temperature was adjusted by an Oxford ITC502S temperature controller. The choice of 5 V was based to the fact that no deviation from linearity in current–voltage curves was observed in the voltage range 1–10 V. For the electrical contact, a coplanar configuration was used (silver, vacuum deposited electrodes, with a distance between them 0.8 mm).

For the conductivity measurements, both the as prepared and the calcinated powders, after their preparation, were pressed into disks, applying a pressure of 30 Bar. The disks were 0.7 mm thick, with a diameter of 10 mm. The electrical conductivity was measured in the temperature ranges 140–440 and 240–440 K, in vacuum (10^{-4} Pa) and in air respectively. Before measurements, the samples were annealed at 440 K for 90 min and left to cool down slowly in order to eliminate persisting effects of previous light exposure. Then, the conductivity was measured after the samples rested in the dark for 24 h at room temperature.

3. Results and discussion

3.1. Structure and morphology

3.1.1. X-ray diffraction

From the XRD patterns (Fig. 1) of the as prepared and calcinated samples the crystalline phase was found to be only anatase [JSPDS No. 021-1272 card] containing

no impurities that may have been caused by the remaining precursor used each time or by the formation of another phase such as rutile. The XRD peaks that correspond to the TiO_2 anatase as prepared nanoplates show an anisotropic growth of the nanocrystals along the c-axis of the anatase lattice [26-28]. This is indicated by the strong peak intensity and narrow width of the (1 0 1) and (2 0 0) reflection and relatively lower intensity and broader width for the (0 0 4) reflection. This suggests that the (0 0 1) surface of the TiO_2 anatase crystal is larger than the (1 0 1) one. Moreover, the XRD narrow peaks that relate to the TiO_2 anatase calcinated nanoplates are equivalent to well defined crystals randomly oriented [29].

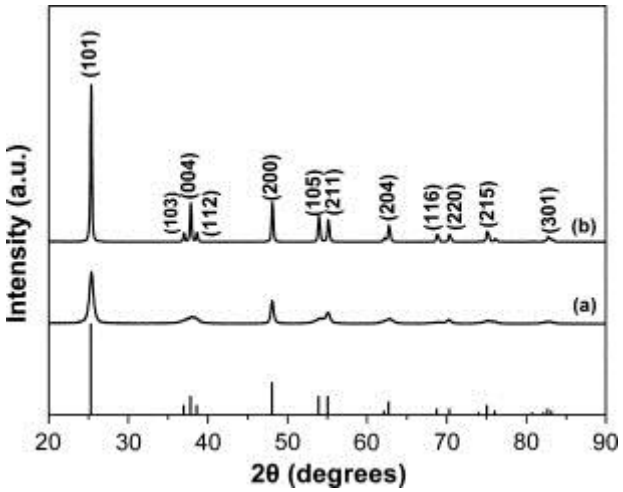

Fig. 1. XRD patterns of the TiO_2 anatase nanopowders, (a) as prepared (b) calcinated at 600 °C.

3.1.2. Transmission electron microscopy (TEM)

The TEM micrographs of the as prepared and calcinated TiO_2 anatase nanoplates are presented in Fig. 2. The calcinated nanoplates have larger dimensions than the washed nanoplates, this observation comes also in agreement with the XRD patterns. More specifically, the large square surface areas of the nanoplates are the {0 0 1} crystal facets and the small isosceles trapezoidal surfaces are the {1 0 1} crystal

facets. The side length of the as prepared nanoplates is ~24 nm and their thickness is ~4 nm (Fig. 2a). As for the calcinated nanoplates the side length is ~33 nm and the thickness is ~25 nm (Fig. 2b). This implies that after the calcination of the samples the {1 0 1} crystal facets of the nanoplates become larger. These observed changes are caused by the heat treatment of the nanoplates where the anatase crystal tends to reach its equilibrium state with the expansion of the energetically favored {1 0 1} crystal facets (0.44 J/m2) and the shrinkage of the relative higher energy {0 0 1} crystal facets (0.90 J/m2) [30].

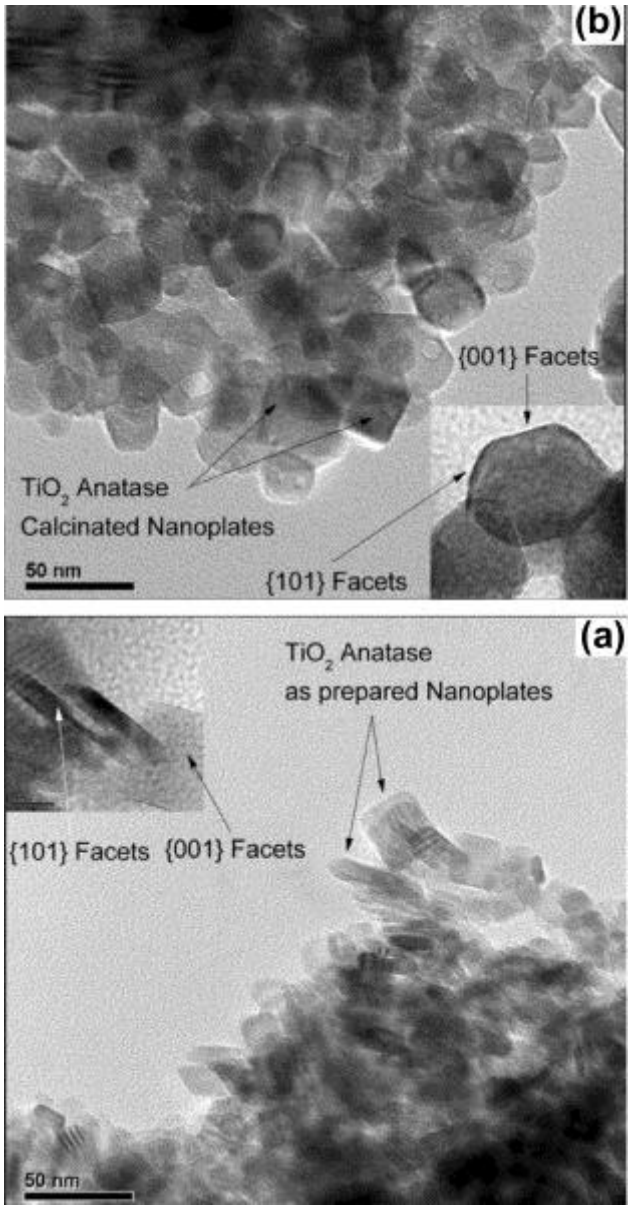

Fig. 2. TEM micrographs of the TiO_2 anatase nanoplates, (a) as prepared (b) calcinated at 600 °C.

3.2. DC conductivity measurements

As it is well known the conductivity of TiO_2 is highly sensitive to the environment [31-33]. The as prepared and the calcinated TiO_2 anatase nanoplates with {0 0 1} facets samples were investigated by temperature dependent conductivity measurements in order to determine their conduction mechanisms in vacuum and in air. The measurements were carried out in the temperature range 150–440 K in vacuum and in 240–440 K in air. For temperatures lower than 240 K, we note that the dark currents in air were smaller than the limit of measurements (<10−14 A).

3.2.1. In vacuum

The temperature dependence of the DC conductivity (σ) in vacuum (10^{-4} Pa), for both the as prepared and the calcinated samples is shown in an Arrhenius type plot of lnσ versus $10^3/T$, illustrated in Fig. 3, revealing the expected semiconductor behavior. The measured σ in vacuum, at 300 K, reaches the values 1.65×10^{-8} and 8.11×10^{-9} Ω^{-1} m^{-1} for the as prepared and the calcinated sample, respectively.

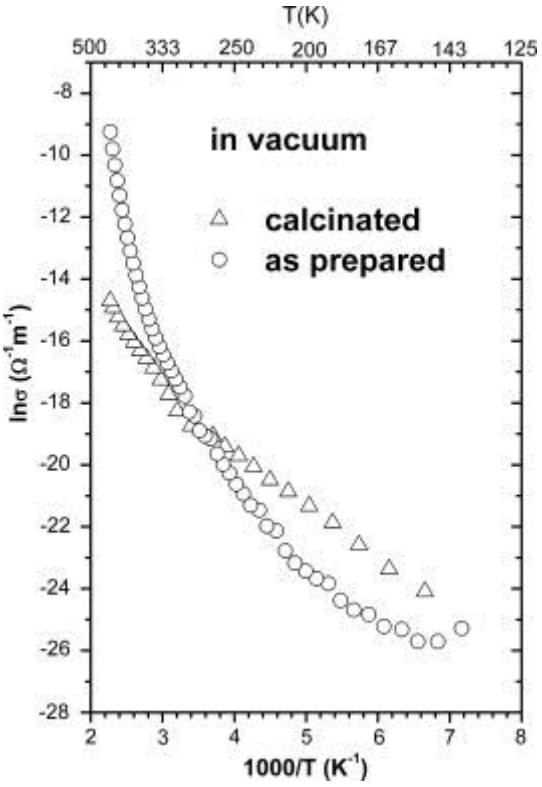

Fig. 3. Temperature dependence of the electrical conductivity versus $10^3/T$ in vacuum, in the temperature range 150–440 K.

The plots of Fig. 3, for both samples, are not linear and this is a reason for looking for other mechanisms of conductivity. Since the investigated semiconducting samples are polycrystalline, one can expect the grain boundary model (GB) to explain the high temperature region of Fig. 3. According to GB model, the interface between grains gives rise to a great concentration of trapping states that are capable of trapping carriers. Consequently, these charged states create a potential energy barrier which impedes the motion of carriers from one crystallite to another and strongly influences the electronic transport between crystallites [34].

Based on GB model we analyze the conductivity behavior of our TiO_2 samples in the high temperature regime. According to Seto [35] and Baccarani et al. [36] the temperature variation of the electrical conductivity of polycrystalline semiconductors depends on the values of three parameters: L, the crystallite size; N_D, the impurities

concentration and E_t, the energy of the trapping states with density N_t. Since it is well known that oxygen vacancies are the most common defects that act as electron donors determining the TiO_2 n-type conductivity, we can suppose a donor concentration N_D.

For any set of values of L, N_D and E_t, there is a characteristic concentration of impurities N_D^* such that if $N_D < N_D^*$ the crystallites are entirely depleted [34]. The barrier height E_b is then given by:

$$E_b = \frac{L^2 e^2 N_D}{8\varepsilon_0 \varepsilon_r} \tag{1}$$

where ε_0 is the vacuum permittivity and ε_r the low frequency permittivity. The conductivity in this case is written as [36]:

$$\sigma = \left[\frac{e^2 L^2 N_C N_D v_C}{2k_B T(N_t - LN_D)}\right] \exp\left(-\frac{E_b}{k_B T}\right) \tag{2}$$

where

$$v_C = \left(\frac{k_B T}{2\pi m^*}\right)^{1/2} \tag{3}$$

with m^* the effective mass of charge carriers and N_C the conduction band effective density of states, given by:

$$N_C = 2\left(\frac{2\pi m^* k_B T}{h^2}\right)^{3/2} \tag{4}$$

Inserting Eqs. (3) and (4) into Eq. (2), we obtain:

$$\sigma = \frac{e^2 L^2 2\pi k_B m^* N_D}{h^3 (N_t - L N_D)} T \exp\left(-\frac{E_b}{k_B T}\right) \quad (5)$$

If $N_D > N_D^*$, the crystallites are partially depleted. When $E_F - E_t - E_b >> k_B T$ the conductivity can be expressed as [35, 36]:

$$\sigma = \frac{e^2 L n_o v_C}{k_B T} \exp\left(\frac{-E_b}{k_B T}\right) = \frac{e^2 L n_o}{(2\pi m^* k_B)^{1/2}} T^{-1/2} \exp\left(-\frac{E_b}{k_B T}\right) \quad (6)$$

where n_o is the electron concentration in the neutral region of crystallites.

The evaluation of the Debye screening length L_D is necessary for the verification of the existence of potential barriers. If $L_D < L/2$, potential barriers exist in the grain boundary region, while if $L_D > L/2$ the transport of electrons occurs without grain boundary scattering. L_D is given as [37]:

$$L_D = \sqrt{\frac{k_B T \varepsilon_0 \varepsilon_r}{e^2 N_D}}$$

To investigate the suitability as well as to determine if the grains are entirely or partially depleted in the high temperature regime we fit our data using Eqs. (5) and (6), respectively. Both plots σT^{-1} and $\sigma T^{1/2}$ versus $10^3/T$ show a linear dependence in the high temperature regime 360–440 K for the as prepared sample and 295–440 K for the calcinated one, suggesting that electrical conduction is controlled by the grain boundary scattering of the charged carriers. A better fitting to our conductivity data is achieved for both samples, using Eq. (6), (Fig. 4a) indicating that grains are partially depleted of charge carriers. From the slopes, activation energies of 1.00 and 0.32 eV were obtained for the as prepared and the calcinated sample, respectively. The last value is in fair agreement with Afifi et al. [38]. The found E_b value of the calcinated

sample is lower, due to its larger crystallite size L, since heat treatment improves the sample's crystallinity. We assumed as L the diameter of the sphere with a volume equal to the volume of the nanoplate. The obtained values of L are 16 and 37 nm for the as prepared and the calcinated sample, respectively. From the calculated activation energies and considering the value of the low frequency permittivity ε_r to be 48 for 100% anatase TiO_2 powders [39], the N_D values of the investigated samples were determined using Eq. (1). The calculated values of N_D are listed in Table 1. The verification of the existence of potential barriers is checked by the evaluation of the Debye screening length L_D. The calculated from Eq. (7)L_D values obey the necessary for the validity of the grain boundary model $L_D < L/2$, in the temperature ranges 360–440 and 295–440 K for the as prepared and the calcinated sample, respectively. Moreover, the ratio L_D/L, using Eqs. (1) and (7), without the need of knowing the values of L and N_D, can be expressed as:

$$\frac{L_D}{L} = \sqrt{\frac{k_B T}{8E_b}}$$

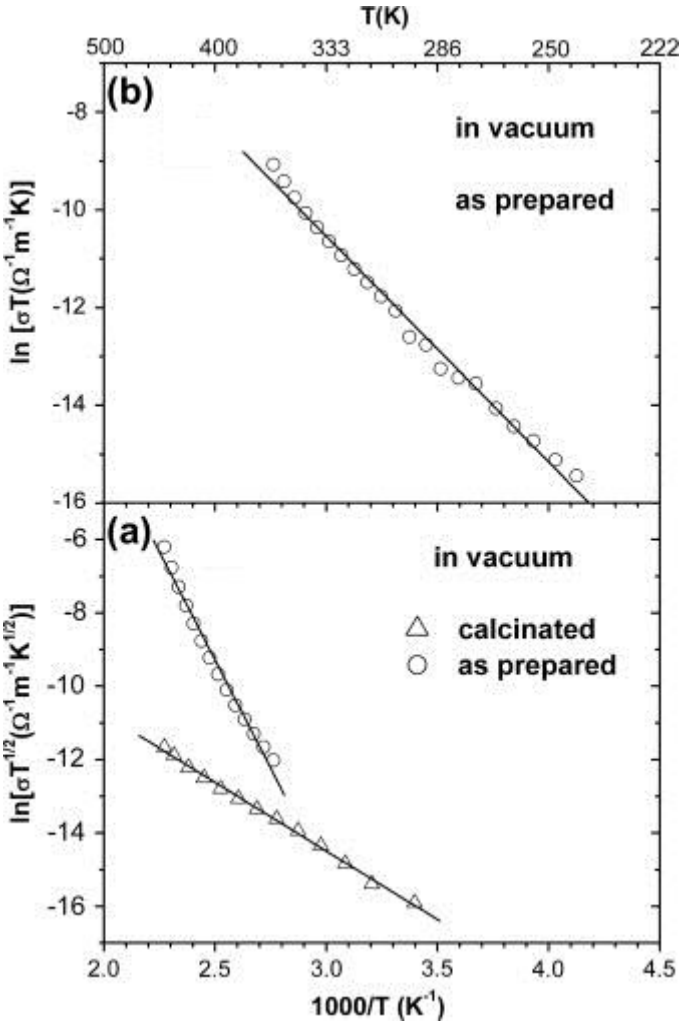

Fig. 4. Temperature dependence in vacuum of (a) ln($\sigma T^{1/2}$) versus $10^3/T$ and (b) ln(σT) versus $10^3/T$. Solid lines are least square fits to the data

Table 1.

Electrical conductivity (σ) at 300 K, barrier height (Eb), donor concentration (ND), Debye screening length (LD), activation energy (W) and Mott parameters (To, N(EF), Whop, R) for TiO_2 with dominant highly reactive {0 0 1} facets samples.

	σ (Ω^{-1} m^{-1}) at 300 K	E_b (eV)	N_D (m^{-3})	L_D (nm)	W (meV)	T_0 (K)	$N(E_F)$ (eV^{-1} m^{-3})	W_{hop} (meV)	R (m)
In vacuum samples									
As-prepared	1.65×10^{-8}	1.00	7.90×10^{25}	At 400 K 1.07	379	9.43×10^{8}	4.22×10^{23}	At 210 K 70.7	At 210 K 2 × 10−8
Calcinated at 600 °C	8.11×10^{-9}	0.32	1.52×10^{25}	At 370 K 2.36		3×10^{8}	1.33×10^{8}	At 210 K 157	At 210 K 1.05×10^{-8}
In air samples									
As-prepared	2.58×10^{-7}	0.45	3.56×10^{25}	At 420 K 1.64		2.32×10^{10}	1.72×10^{22}	At 251 K 531	At 251 K 2.97×10^{-8}
Calcinated at 600 °C	1.19×10^{-9}	0.62	9.45×10^{24}	At 420 K 3.19		3.94×10^{10}	1.00×10^{22}	At 264 K 630	At 264 K 3.35×10^{-8}

This ratio is smaller than ½ in the above mentioned temperature ranges, ensuring the validity of the grain boundary model. The L_D values for both samples are given in Table 1.

In the temperature range 240–360 K a second mechanism controls the electrical conduction of the as prepared sample. To investigate if small polaron hopping model (SPH) [40] can describe this conduction mechanism and to determine if SPH is adiabatic or non adiabatic, $\ln(\sigma T)$ and $\ln(\sigma T^{3/2})$ versus $1000/T$ have been plotted. SPH is adiabatic when the probability for the polaron to hop to adjacent sites is high. An exponential dependence of σT on $1000/T$ is predicted in this case, expressed by:

$$\sigma = (\sigma_0/T)\exp(-W/k_BT) \quad (8)$$

where *W* is the activation energy and σ_0 the pre-exponential factor.

When this probability is small, SPH is non adiabatic and conductivity obeys to an exponential dependence of $\sigma T^{3/2}$ on 1000/*T*, given as:

$$\sigma=(\sigma_0 T^{-3/2})\exp(-W/K_B T) \quad (9)$$

Our conductivity data show a better fitting in the adiabatic regime (Fig. 4b). The value of the activation energy *W*, determined from the slope of the plot is listed in Table 1.

The plots presented in Fig. 3 display a region for temperatures below 240 and 295 K for the as prepared and the calcinated sample, respectively, corresponding to a different conduction mechanism. Looking for the suitable conduction mechanism in these temperature regimes, the conductivity data were analyzed using the variable range hopping conduction model (VRH) proposed by Mott [40]. According to this model, when the density of states is finite and the states are localized, the conduction mechanism obeys to the relation:

$$\sigma = \sigma_0 T^{-1/2} \exp\left[-\left(\frac{T_0}{T}\right)^{1/4}\right] \quad (10)$$

where

$$\sigma_0 = \frac{3e^2 \nu}{(8\pi)^{1/2}} \left[\frac{N(E_F)}{\alpha k_B}\right]^{1/2} \quad (11)$$

$N(E_F)$ is the density of the localized states at the Fermi level, α is the inverse of the localization length, ν is the typical phonon frequency and T_0 is a characteristic temperature which depends on the density of states at the Fermi level and represents a measure of disorder in the material [41].

Thus, the $\ln(\sigma T^{1/2})$ plots versus $T^{-1/4}$, in the temperature range 150–295 and 165–240 K for the calcinated and the as prepared samples respectively, are shown in Fig. 5, according to Eq. (10). The characteristic temperatures T_0 are obtained from the slopes

of the linear fits of Fig. 5 and $N(E_F)$ are calculated using Eq. (12). The inverse of the localization length is assumed to be 0.124 $Å^{-1}$[42].

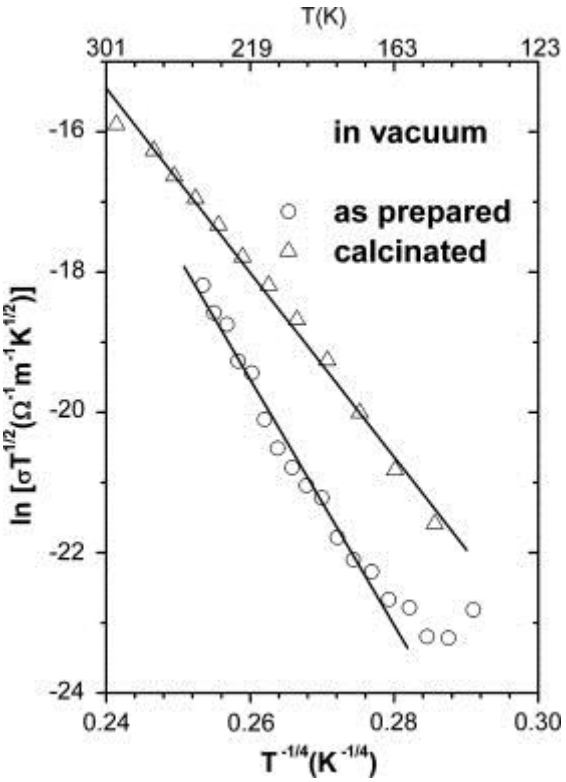

Fig. 5. Plot of $\ln(\sigma T^{1/2})$ as a function of $T^{-1/4}$ in vacuum and the linear regression fits.

The mean hopping distance R between sites and the average hopping energy W_{hop} required for hopping are given by [40]:

$$R = \left[\frac{9}{8\pi N(E_{\mathrm{F}})\alpha k_{\mathrm{B}}T}\right]^{1/4} \tag{13}$$

$$W_{\mathrm{hop}} = \frac{3}{4\pi R^3 N(E_{\mathrm{F}})} \tag{14}$$

The values of T_0, $N(E_F)$, as well as of W_{hop}, and R at 210 K, estimated by Eqs. (12)-(14) are collected in Table 1.

The obtained values of W and R at T = 210 K satisfy the Mott's requirements $\alpha R \geqslant 1$ and $W_{hop} > k_B T$ for both samples.

3.2.2. In air

The temperature dependence of the conductivity in air, plotted as $\ln\sigma$ versus $10^3/T$, is illustrated in Fig. 6, for both samples in the temperature range 240–440 K, revealing a different behavior from that in vacuum. The conductivity of the samples in air shows a decrease with temperature in the ranges 300–370 and 285–330 K for the as prepared and the calcinated sample, respectively. Since it is observed only in air, it might be associated with oxygen in air [43]. The conductivity values in air, at 300 K, are $2.58 \times 10^{-7}\ \Omega^{-1}\ m^{-1}$ and $1.19 \times 10^{-9}\ \Omega^{-1}\ m^{-1}$ for the as prepared and the calcinated sample, respectively. These values are about an order of magnitude smaller than the corresponding values in vacuum. It is known that two competing mechanisms take place in air: the oxygen adsorption and the water adsorption [44]. The first one causes a decrease in dark conductivity due to the oxygen gas molecules which capture electrons from the conduction band and the donor states to form O_2^-. The second increases the conductivity and this can be attributed to the water dissociation on the anatase TiO_2surface which may dope the material by proton insertion and Ti^{3+} formation. It is evident that the oxygen adsorption finally dominates in these samples.

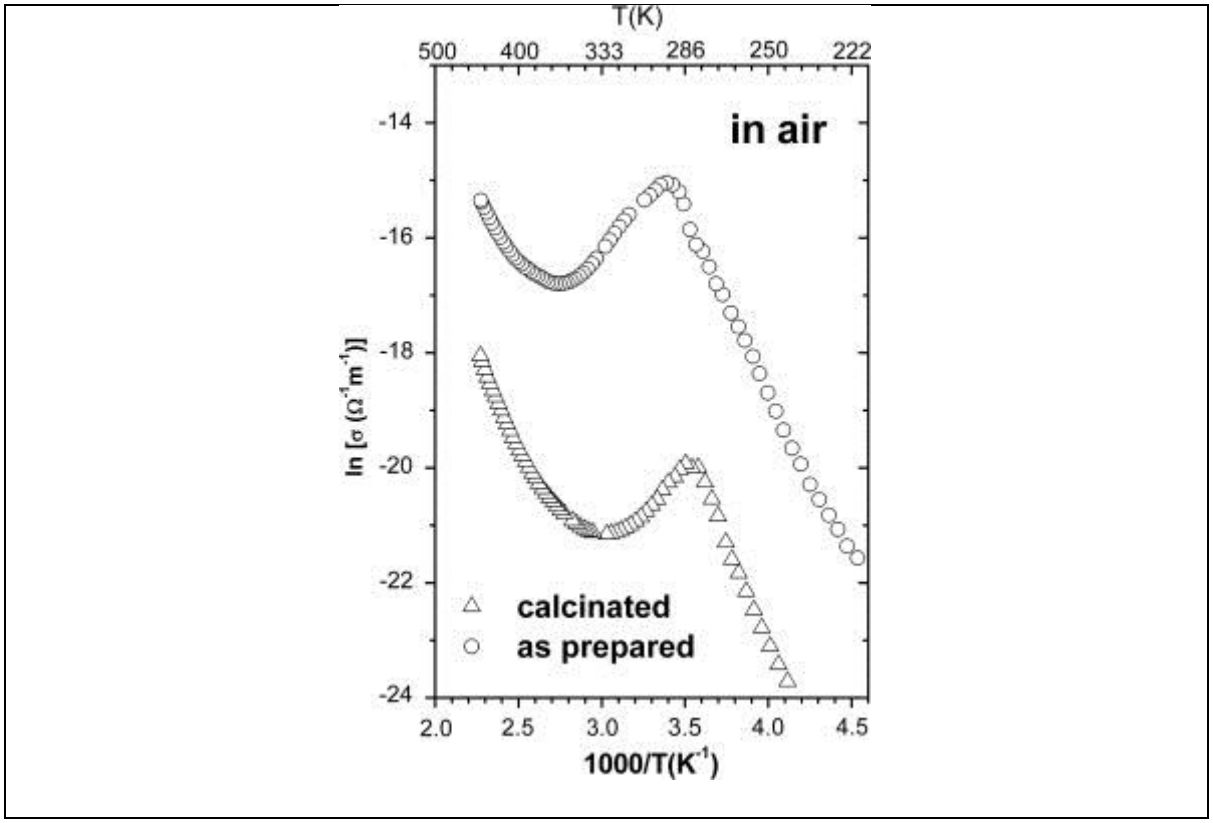

Fig. 6. Temperature dependence of the electrical conductivity versus $10^3/T$ in air in the temperature range 240–440 K.

In the high temperature regime, between 400 and 440 K, a semiconductor character for both samples is identified. The temperature dependence of electrical conductivity was analyzed by grain boundary model and the plots $\ln(\sigma T^{-1})$ and $\ln(\sigma T^{1/2})$ versus $10^3/T$ show that in this temperature range the experimental data obey to a linear fit for both samples, in accordance to Eqs. (5) ; (6). The better fitting is obtained in Fig. 7, indicating that grains are partially depleted of charge carriers. The calculated values of E_b, N_D and L_D at 420 K in air are listed in Table 1. The L_D values satisfy the necessary for the validity of grain boundaries condition $L_D < L/2$ for both samples.

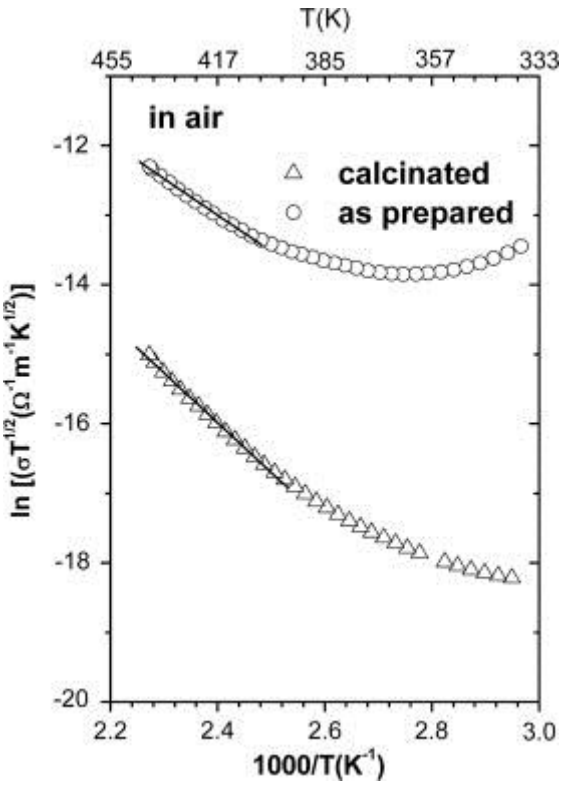

Fig. 7. Plot of $\ln(\sigma T^{1/2})$ as a function of $10^3/T$ in air and the linear regression fits.

At the low temperature regime 220–285 K for the as prepared sample and 240–280 K for the calcinated one, the data were fitted in the (VRH) model. The temperature dependence of the electrical conductivity, plotted as $\ln(\sigma T^{1/2})$ versus $T^{-1/4}$ for both samples, is shown in Fig. 8. The observed linearity confirms the VRH conduction. The values of T_0 obtained from the slope of the linear fit of Fig. 8, $N(E_F)$, as well as of W_{hop} and R at 251 and 264 K for the as prepared and the calcinated sample respectively are listed in Table 1.

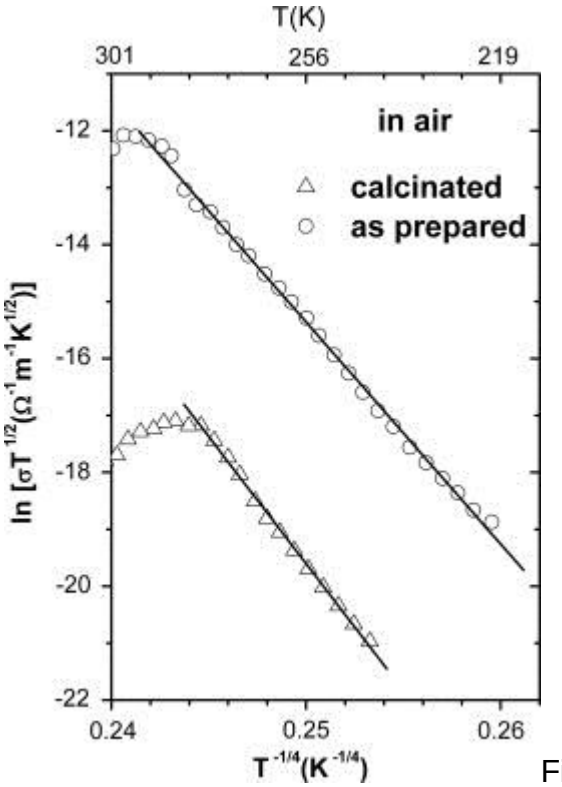

Fig. 8.

Fig. 8. Temperature dependence of ln($\sigma T^{1/2}$) versus $T^{-1/4}$ in air. Solid lines are least square fits to the data.

The obtained values of R in air, as well as the values of W_{hop} calculated at 251 and 264 K for both samples, satisfy the Mott's requirements $\alpha R \geqslant 1$ and $W > k_B T$.

4. Conclusions

In this work, the electrical properties of titanium dioxide anatase nanoplates with dominant high reactive {0 0 1} facets have been investigated in vacuum and in air. The samples were obtained by a solvothermal method and two kinds of them, as prepared and calcinated at 600 °C were studied. The samples are polycrystalline with anatase structure. We have shown that the conduction mechanism in the samples is different in the high and low temperature regime. In vacuum, two at least main conduction mechanisms were observed. In the high temperature regime the conductivity was controlled by partially depleted of charge carriers grains, while one more conduction

mechanism, the adiabatic SPH, was suggested by the temperature dependence in the case of the as prepared sample. The conductivity at low temperatures exhibited VRH conduction. In air, the conductivity values are one order of magnitude lower than those in vacuum, indicating that air causes the adsorption of oxygen molecules. A decrease of conductivity with temperature is observed in air in the ranges 300–370 and 285–330 K for the as prepared and the calcinated sample, respectively. The conduction process in air, beyond these temperature ranges is controlled by partially depleted of charge carriers grains and VRH. These experimental results might improve future applications based on the better understanding of the role of the environment on the electrical properties of anatase TiO_2 with dominant highly reactive {0 0 1} facets.

References

[1] U. Diebold, Appl. Phys. A 76 (2001) 1.

[2] S. Reham, R. Ullah, A.M. Butt, N.D. Gohar, J. Hazard. Mater. 170 (2009) 560.

[3] K. Pomoni, A. Vomvas, N. Todorova, T. Giannakopoulou, T. Mergia, C. Trapalis, J. Alloys Comp. 509 (2011) 7253.

[4] M. Asiltürk, F. Sayilkan, E. Arpac, J. Photochem. Photobiol. A 203 (2009) 64.

[5] G.Q. Wang, W. Lan, G.J. Han, Y. Wang, Q. Su, X.Q. Liu, J. Alloys Comp. 509 (2011) 4150.

[6] R. Asahi, T. Morikawa, T. Ohwaki, K. Aoki, Y. Taga, Science 293 (2001) 269.

[7] J.C. Yu, J.G. Yu, W.K. Ho, Z.T. Jiang, L.Z. Jiang, Chem. Mater. 14 (2002) 3808.

[8] T. Umebayashi, T. Yamaki, H. Itoh, K. Asai, Appl. Phys. Lett. 81 (2002) 454.

[9] J. Yu, S. Liu, Z. Xiu, W. Yu, G. Feng, J. Alloys Comp. 488 (2009) 314.

[10] C.M. Teh, A.R. Mohamed, J. Alloys Comp. 509 (2011) 1648.

[11] J.I.L. Chen, G. von Freymann, S.Y. Choi, V. Kitaev, G.A. Ozin, Adv. Mater. 18 (2006) 1915.

[12] C. Aprile, A. Corma, H. Garcia, Phys. Chem. Chem. Phys. 10 (2008) 769.

[13] G. Ruani, C. Ancora, F. Corticelli, C. Dionigi, C. Rossi, Sol. Energy Mater. Sol. C 92 (2008) 537.

[14] W. Zhang, D. Zhang, T. Fan, J. Gu, J. Ding, H. Wang, Chem. Mater. 21 (2009) 33.

[15] K. Lv, J. Yu, L. Cui, S. Chen, M. Li, J. Alloys Comp. 509 (2011) 4557.

[16] J. Zhang, J. Wang, Z. Zhao, T. Yu, J. Feng, Y. Yuan, Z. Tang, Y. Liu, Z. Li, Z. Zou, Phys. Chem. Phys. 14 (2012) 4763.

[17] S. Liu, J. Yu, B. Cheng, M. Jaroniec, Adv. Colloid Interface 173 (2012) 35.

[18] L. Xi, J. Zhou, H. Li, Catal. Commun. 24 (2012) 20.

[19] J. Zhang, W. Chen, J. Xi, Z. Ji, Mater. Lett. 79 (2012) 259.

[20] A.S. Ichimura, B.M. Mack, S.M. Usmani, D.G. Mars, Chem. Mater. 24 (2012) 2324.

[21] H. Yu, B. Tian, J. Zhang, Chem. Eur. J. 17 (2011) 5499.

[22] S. Liu, J. Yu, M. Jaroniec, Chem. Mater. 23 (2011) 4085.

[23] Y.B. Li, Y. Bando, D. Golberg, K. Kurashima, Appl. Phys. Lett. 82 (2002) 5084.

[24] T. Sasaki, Y. Ebina, T. Tanaka, M. Harada, M. Watanabe, G. Decher, Chem. Mater. 13 (2001) 4661.

[25] A.J. Frank, N. Kopidakis, J. Van de Lagemat, Coord. Chem. Rev. 248 (2004) 1165.

[26] M.V. Sofianou, C. Trapalis, V. Psycharis, N. Boukos, T. Vaimakis, J.G. Yu, W.G. Wang, Environ. Sci. Pollut. Res. (2012), accepted for publication, http://dx.doi.org/10.1007/s11356-012-0747-x.

[27] C. Greaves, J. Appl. Cryst. 18 (1985) 48.

[28] J.I. Langford, D. Louër, J. Appl. Cryst. 15 (1982) 20.

[29] Th E. Weirich, M. Winterer, S. Seifried, H. Hahn, H. Fuess, Ultramicroscopy 81 (2000) 263.

[30] H.G. Yang, C.H. Sun, S.Z. Qiao, J. Zhou, G. Liou, S.C. Smith, H.M. Cheng, G.Q. Lu, Nature 453 (2008) 638.

[31] B. Huber, H. Gnaser, Chr Ziegler, Surf. Sci. 566–568 (2004) 419.

[32] A. Rothschild, F. Edelman, Y. Komen, F. Komen, Sens. Actuators B Chem. 67 (2000) 282.

[33] K. Pomoni, A. Vomvas, Chr. Trapalis, Thin Solid Films 479 (2005) 160.

[34] A. Adam, L.A. Wahab, K. Sedeek, Mater. Chem. Phys. 79 (2003) 15.

[35] J.Y.W. Seto, J. Appl. Phys. 46 (1975) 5247.

[36] G. Baccarani, B. Ricco, G. Spandini, J. Appl. Phys. 49 (1978) 5565.

[37] J.W. Orton, M.J. Powel, Rep. Prog. Phys. 43 (1980) 1263.

[38] M.A. Afifi, M.M. Abdel-Aziz, I.S. Yahia, M. Fadel, L.A. Wahab, J. Alloys Comp. 455 (2008) 92.

[39] L.A. Harris, J. Electrochem. Soc. Solid State Sci. Technol. 127 (1980) 2657.

[40] N.F. Mott, E.A. Davis, Electronics Process in Non-Crystalline Materials, Clarendon Press, Oxford, 1979.

[41] A. Yildiz, S.B. Lisesivdin, M. Kasap, Diana Mardare, J. Mater. Sci. Electron. 21 (2010) 692.

[42] S. Mahadevan, A. Giridhar, K.G. Rao, J. Phys. C 10 (1977) 4499.

[43] C.A. Amorim, O.M. Berengue, H. Kamimura, E.R. Leite, A.J. Chiquito, J. Phys.: Condens. Matter 23 (2011) 205803.

[44] K. Pomoni, A. Vomvas, Chr. Trapalis, Thin Solid Films 516 (2008) 1271.